POLITECNICO DI TORINO

Department of Energy "Galileo Ferraris"
Master of Science in Energy and Nuclear Engineering

NUMERICAL APPROACH TO SIMULATE THERMAL-MHD COUPLED FLIBE FLOWS IN THE ARC FUSION REACTOR

Supervisors:

Prof. Massimo Zucchetti
Raffaella Testoni

Co-Supevisors:

Prof. Zachary Hartwig
Caroline Sorensen

Candidate:

Edoardo Andrea Prato

Tesi di Laurea Magistrale
Anno Accademico 2018/2019
Sessione di Marzo

Sommario

Da decenni, la fusione nucleare viene studiata dalla comunità scientifica internazionale: questo per via del suo grande potenziale. Essa infatti consentirebbe la produzione di grandi quantità di energie pulite ed esenti da emissione di gas serra.
Svariati sono i modelli di reattori a fusione già sperimentati o prossimi alla costruzione. Presso il Plasma Science and Fusion Center (PSFC) del Massachusetts Institute of Technology un design innovativo è stato di recente proposto: ARC, Affordable Robust Compact reactor.
ARC presenta la peculiarità di avere dimensioni ridotte e questo è dovuto principalmente all'utilizzo di magneti superconduttori ad alta temperatura. Un altro elemento che lo contraddistingue è rappresentato dalla presenza di un blanket attraversato dal sale fuso Lithium-Fluoride, Beryllium-Fluoride (FLiBe) che assolve la funzione di refrigerante, schermatura dei neutroni e generatore di trizio. Esso è caratterizzato da una temperatura di ebollizione molto elevata (circa 1700 K) il che garantisce un flusso di tipo monofase. Essendo il FLiBe un conduttore elettrico, sarà soggeto a fenomeni di tipo magnetoidrodinamico (MHD).
Il moto del fluido all'interno dei canali del blanket risulta complesso e caratterizzato da elevate cadute di pressione. La valuzatione di profili di velocità, cadute di pressione e flussi termici è di particolare interesse nella progettazione del blanket.
In questo contesto, è necessario condurre un'analisi dei fenomeni legati alla magnetoconvezione, attraverso il supporto di codici di calcolo. Dopo una breve introduzione su ARC e una descrizione dei fondamenti teorici sulla magnetoidrodinamica (Capitoli 1 e 2), il Capitolo 3 presenta al lettore l'approccio di tipo numerico adottato e l'implementazione dei codici per l'analisi CFD in ambienti OpenFoam e COMSOL. Nel Capitolo 4 vengono presentati i risultati per un particolare tipo di geometria per cui sono disponibili risultati analitici in letteratura. Infine, il Capitolo 5 presenta un riassunto dei principali risultati numerici ottenuti e le attività future che verranno svolte sulla base di questo lavoro.

Abstract

For decades, nuclear fusion energy has been pursued by scientist worldwide. This is because fusion energy devices have the potential produce huge amounts of clean carbon-free energy. Different designs for fusion reactors have been proposed and some build. At the Plasma Science and Fusion Center (PSFC) of the Massachusetts Institute of Technology (MIT) an innovative design was created: ARC, the Affordable Robust Compact reactor.
ARC achieve its compactness partially due to the presence of High Temperature Superconductors (HTS) for the magnetic confinement and the use of molten salt Lithium-Fluoride, Beryllium-Fluoride (FLIBE) as coolant, neutron shield, and tritium breeder. It has the characteristic of extremely high boiling point (about 1700 K) which guarantees a single-phase flow. As an electrical conducting fluid, MHD flows can be encountered in FLiBe.
The flow inside breeding blanket channels can be very complex and results in high pressure drops, especially when the channels are also made by electrically conducting materials. The knowledge of fluid velocity profile, pressure drop and prediction of thermal heat fluxes are of considerable interest for blanket design.
For this purpose, thermal-MHD simulation can be run. The codes evaluate 3D transient problems in which the quantities describing the problem have to be evaluated at each discretized point of the geometry domain.
After a brief introduction of ARC and the fundamentals of MHD (Chapters 1 and 2), Chapter 3 will present the numerical approach adopted and the implementation of thermal-MHD coupled code on Open-FOAM and COMSOL, as well as a stability discussion. In Chapter 4 the results of such simulations are presented, with sections dedicated to comparison between codes and analitycal results for a simple class of problem: square ducts. Finally Chapter 5 will conclude this thesis work with special attention on future code implementation and experiments to be performed.

Acknowledgments

I would like to thank my supervisors Prof. Massimo Zucchetti and Prof. Zach Hartwig, as well as Prof. Dennis Whyte for the wonderful opportunity they gave me. I want to express my infinite gratitude especially to assistant professor Raffaella Testoni the PhD students Caroline Sorensen, Luigi Candido and Stefano Segantin for their precious help. This few months spent at MIT were very useful for my personal growth, I could increase my knowledge about fusion and I worked with incredible people. I wish I could contribute more in the future by continuing working on PSFC projects.

Contents

Chapter 1

Introduction

In a D-T fusion powered reactor, the breeding blanket plays a key role for heat removal, neutron shielding and tritium breeding.
Since we are dealing with a magnetically confined tokamak, magnetohydrodynamic (MHD) effects on the coolant can not be prevented. The flow of a conducting fluid can vary significantly when subjected to external magnetic fields.
After giving a general overview of the reactor, this thesis will focus on the behavior of the molten salt FLiBe (LiF-BeF_2). It is the coolant candidate chosen for ARC fusion reactor [1]. FLiBe is characterized by a relatively low electrical conductivity compared, for example, to the liquid eutectic PbLi alloy chosen for others device designs in the fusion community.
The next chapters will illustrate the general theory which govern magnetohydrodynamics and the way to numerically treat MHD. Simulations are then conducted in order to model the fundamental MHD cases applied to ARC reactor.

1.1 Background on thermonuclear fusion

A fusion reaction is the phenomenon involving two or more nuclei that combine together forming as products another nucleus and/or other subatomic particles. Fig.1.1 shows the DT fusion reaction.

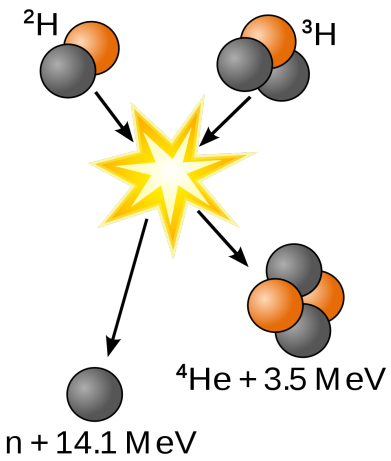

Figure 1.1: Nuclear fusion reaction [5]

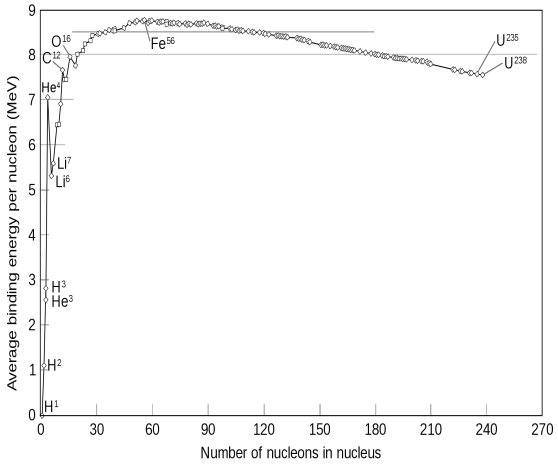

Figure 1.2: Binding energy as a function of atomic mass [5]

As we can see in figure 1.2, we can fuse very light nuclei in order to gain a huge amount of energy per reaction. Several reactants and their reactions have been investigated by the scientific community during the last decades. This effort has identified three as the most promising fuels: deuterium (D), tritium (T) both of which are hydrogen isotopes, and helium-3 (^{3}He). Among all the possible fusion reactions, the most common ones are the following [3]:

$$D + T \rightarrow {}^4He + n + 17.6MeV \tag{1.1}$$

$$T + T \rightarrow {}^4He + 2n + 11.3MeV \tag{1.2}$$

$$D + D \rightarrow {}^3He + 1n + 3.2MeV \tag{1.3}$$

$$D + D \rightarrow T + p + 4.0MeV \tag{1.4}$$

$$D + {}^3He \rightarrow {}^4He + p + 18.3MeV \tag{1.5}$$

The D - T reaction (Eq.1.1) requires a lower temperature (on the order of 15 keV which means about 175 millions Kelvin) [3] to achieve an appreciable reaction rate. A 3.5 MeV alpha and 14.1 MeV neutron are produced, which introducing the requirement to extract heat and to shield the other components (HTS magnets work at cryogenic temperatures), but also to the possibility to exploit neutron flux irradiating Lithium in order to produce T *in situ*.
In fact, while deuterium can be found in water in appreciable natural amount (around 1 deuterium atom in 6700 atoms of hydrogen [6]), tritium cannot be found in nature, it is also radioactive with a 12.3 years half life, hence the ability to produce it is essential to have a self-sustained reactor.

1.2 Magnetic confinement in Tokamaks

In the last decades, several confinement concepts have been investigated. The main challenge is to shape and confine the very high temperature plasma (about 100 millions degree K) and keep it far away from the walls. A great attention has been given to magnetic-confinement devices such as the Tokamak and the Stellarator.
Pros and cons and technical limitations are present in each configuration: on one hand the Stellarator promise to achieve higher temperatures, so that we can think to use different fuels than deuterium and tritium (D-T reactors). On the other hand, issues on plasma stability make Stellarators more technologically challenging than Tokamaks. Tokamaks became the dominant concept in fusion research and spread worldwide. Fig.1.3 shows the basic Tokamak configuration. One can distinguish three different magnets: central solenoid, poloidal field coils, toroidal field coils. The first one serves as a heating device (Ohmic heating) and to induce the toroidal plasma current. The second one is devoted to shape the plasma. Finally, the toroidal (D-shape) coils (TFC), play the key role to confine the plasma and keep it far enough from the walls[3].

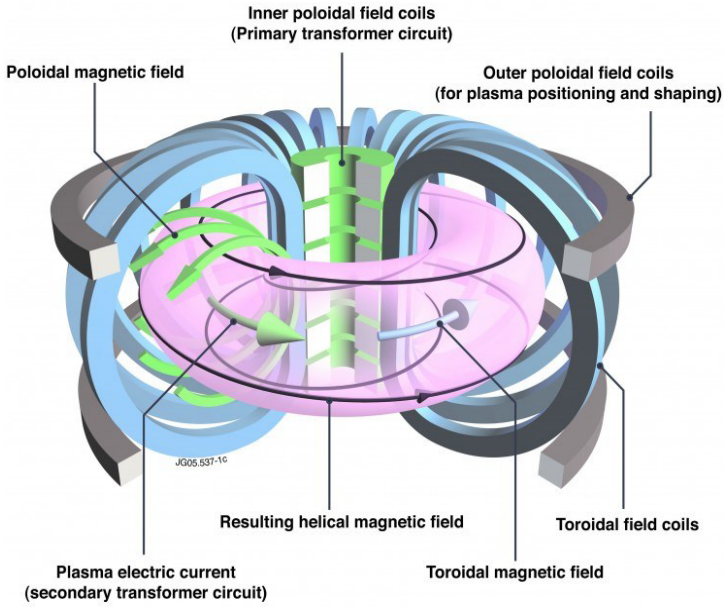

Figure 1.3: Tokamak magnetic confinement [4].

On one hand, the use of HTS superconductor allow us to apply very strong magnetic field. This means that we can achieve high power densities and reduce the dimensions. On the other hand, the presence of strong magnetic fields increase the MHD effect for the conductive coolant flowing within the TF coils.

1.3 The ARC project

The ARC (Affordable, Robust, Compact) fusion reactor is a tokamak designed by researchers at the Plasma Science and Fusion Center of the Massachusetts Institute of Technology. One goal of this conceptual design is to minimize the reactor size which immediately reflects in technical and economic advantages.
The way to achieve the reduction in size is the introduction of a technology innovation such as high temperature superconductors (HTS), that allow high values of magnetic fields [1]. This can be seen by the fusion power and density $[W/m^3]$ expression, which is related to the toroidal magnetic B_T

$$\frac{P_f}{V_p} \propto B_T^4 \tag{1.6}$$

ARC's toroidal magnetic field is designed to be 9.2T at the axis, implying that, the maximum value a the inboard wall will be 23 T. Compared to ITER, ARC promises to achieve a similar fusion power with $1/8^{th}$ smaller dimensions.

Several other innovative features can be highlighted:

- plasma energy gain factor Q>10, which represent the ratio between the fusion power and the plasma external heating. Very ambitious value if we think at the compact reactor size (major radius about 3.3 m)
- demountable toroidal field coils which allow modular replacement of interior components, and the entire vacuum vessel.

- The vacuum vessel will be entirely immersed in a FLiBe bath. An high-temperature, single-phase, low-pressure fluid which acts as neutron moderation, heat removal, shielding and capture for efficient tritium breeding.

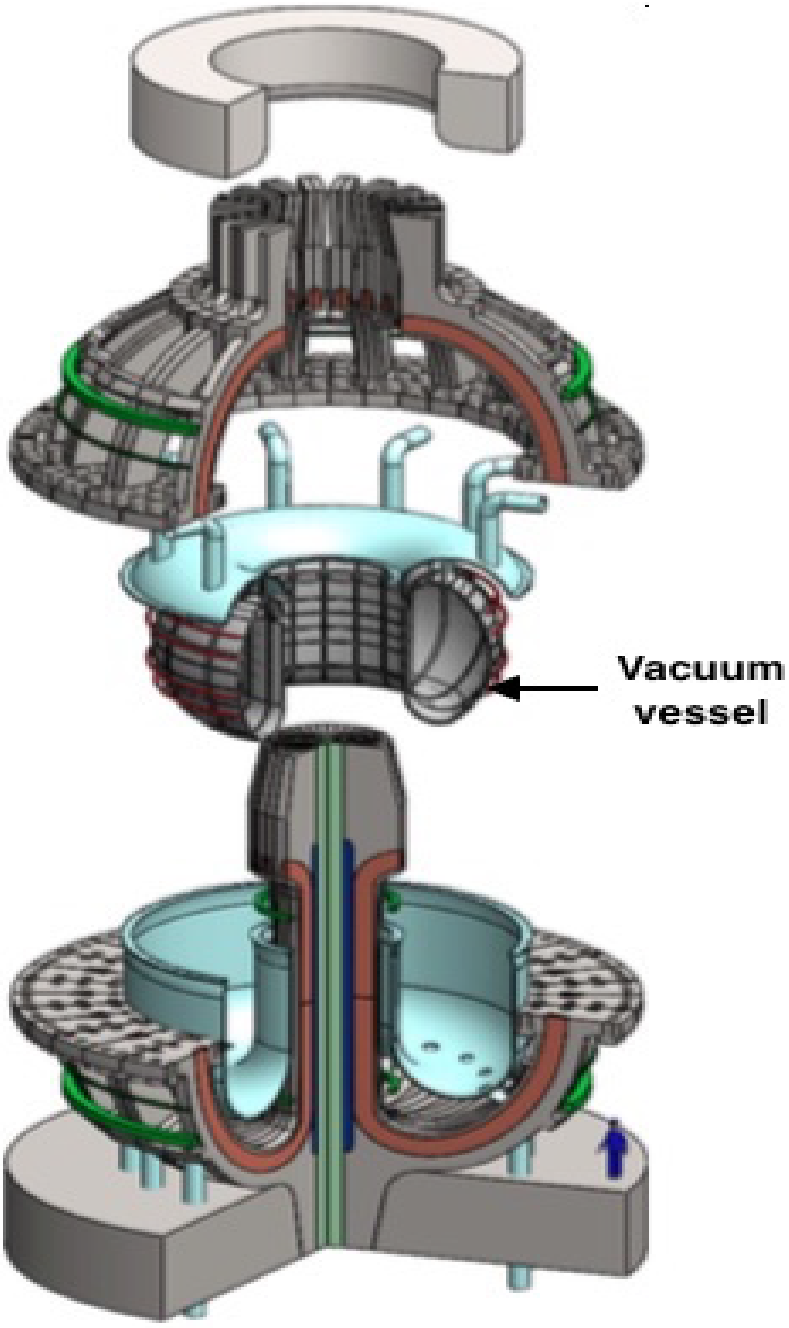

Figure 1.4: Single piece vacuum vessel [1].

1.4 The breeding blanket of ARC

The breeding blanket is the reactor component mainly devoted to removing the heat, shielding the surrounding superconducting magnets and and to producing tritium inside the fusion reactor. One option to do that, is to let the 14 MeV neutrons coming from the D-T reaction interact with lithium, via the reaction shown in equations below.

$$n + {}^{6}Li \rightarrow {}^{4}He + T + 4.78MeV \tag{1.7}$$

$$n + {}^{7}Li \rightarrow {}^{4}He + T + n - 2.47MeV \tag{1.8}$$

Eq.1.7 is of particular interest because of its exothermic behavior. Natural lithium is present with about 93% ^{6}Li. It means that lithium has to be enriched in ^{6}Li. However, this can not guarantee a TBR, which is the ratio between the tritium produced and the 14 MeV fusion neutrons, larger than 1, which is of great importance in order to maintain the fuel cycle. Hence, to increase TBR, a layer of Beryllium which acts as a neutron multiplier can be included in the blanket.
Several breeding blanket concepts has been proposed. As far as the liquid ones are concerned, two fluids, both electrical conducting, have been considered for this purposes:

- FLiBe, which is a molten salt characterized by low conductivity and high Prandtl number.
- PbLi, high conductivity, low Prandtl number.

In the ARC conceptual design, FLiBe has been chosen. In figure 1.5 we can see how the ARC cooling system is thought. The vaccum vessel (VV) is cooled by forced flow by four sections: the upper and lower outer divertors (purple and blue lines), the inboard and outboard sides of the VV main chamber which are represented by the yellow and orange lines respectively. FLiBe is proposed to enter this channels at 800 K, in order to stay far from to freezing point. Subsequently it exits this channel into the surrounding FLiBe tank and moves toward the top by natural convection flow. Here, the hot FLiBe is extracted by the red pump and direct the the heat exchanger to close the thermal cycle. Although the system appears complex, it has the great advantage of flexibility: it is designed to extract very high heat fluxes, but can be easily modulated for low thermal loads. The FLiBe that is not pumped into the cooling channels is pumped directly into the FLiBe tank by the recirculating pump (black line) ion order maintain the total flow rate constant.
In the study of ARC a 525 MW of fusion power is produced in nominal condition. This will result in a flux of 2.2×10^{20} 14.1 MeV neutrons per second, hence a total of 484 MW of volumetric heating is produced by neutrons interactions in the surrounding structure. In particular 227 MW of this is deposited in the VV (structural material + FLiBe cooling) while the rest is deposited in the blanket FLiBe tank. Moreover, the core plasma will radiate about 50 MW, which is 35% of the plasma heating power (alpha + external heating) to the VV main chamber walls. The remaining 65% will reach the two outer divertors [1].

In the next chapters, the fluid behavior subjected to such thermal loads and magnetic fields will be discussed and how MHD influences the flow in term of pressure drop and heat exchange.

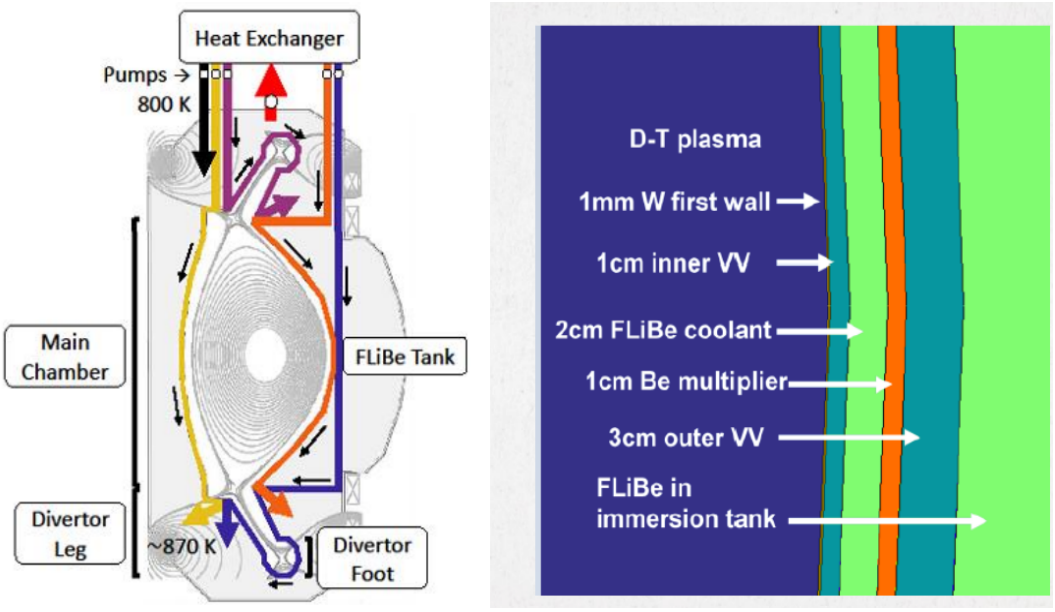

Figure 1.5: ARC cooling system [2].

Chapter 2

Theoretical Background

In the following sections, MHD thermofluid phenomena and the governing equations for a laminar and incompressible flow are explained. Three fundamental papers of MHD studies are considered: Hartmann flow (1936) [7], Shecliff flow (1953) [10] and Hunt flow (1965) [11]. For those type of problems, exact solution can be provided (Appendix A), and numerical codes can be compared to. This outline of the concepts draws on Davidson (2001) [8] and Müller and Büler (2001) [9].

2.1 MHD equations

A magnetohydrodynamic flow occurs whenever an electrically conductive fluid flows in the presence of a magnetic field. Besides the conventional equations of motion we also have to consider the electromagnetic equations, in particular the reduced Maxwell equations for moving conductors. The governing equations for an incompressible MHD flow are:

$$\nabla \cdot \vec{j} = 0 \qquad \text{Charge conservation} \tag{2.1}$$

$$\nabla \cdot \vec{B} = 0 \qquad \text{Solenoidal nature of } \vec{B} \tag{2.2}$$

$$\nabla \times \vec{E} = -\frac{\partial \vec{B}}{\partial t} \qquad \text{Faraday's law} \tag{2.3}$$

$$\nabla \times \vec{B} = \mu \, \vec{j} \qquad \text{Ampere's law} \tag{2.4}$$

$$\vec{j} = \sigma \, (\vec{E} + \vec{u} \times \vec{B}) \qquad \text{Ohm's law for moving conductors} \tag{2.5}$$

$$\vec{F} = \vec{j} \times \vec{B} \qquad \text{Lorentz force} \tag{2.6}$$

Where $\vec{j}, \vec{E}, \vec{B}, \mu, \sigma, \vec{u}$ and $\vec{F}$ stand for current density [A/m^2], electric field [V/m], magnetic field [T], magnetic permeability [H/m], electrical conductivity [S/m], velocity field [m/s] and Lorentz force per unit volume [N/m^3], respectively.
When a conducting fluid flows perpendicular to a imposed magnetic field $\vec{B_0}$, a chain of events can be observed:

1. An electromagnetic force of the order of $|\vec{u} \times \vec{B}|$ arise and, immediately, an electric current is generated by (2.5).

2. These currents, according to (2.4) result on generation of secondary (induced) magnetic field $\vec{b}$ giving $\vec{B} = \vec{B_0} + \vec{b}$. The induced magnetic field lines are in the same direction of the conductor (fluid) motion, in such a way that it appears that the fluid drags the magnetic field lines.

3. These two magnetic field (imposed and induced) interact with the current according to (2.6) giving rise to the Lorentz forces. Such forces, especially in the case of a fluid moving inside an electrically conducting duct, act as an obstacle for the motion and will result in an high pressure drop.

By combing equations(2.1 - 2.5), and defining the new variable $\eta = \frac{1}{\sigma\mu}$ it yields to an equation for the transport of the $\vec{B}$ field

$$\frac{\partial \vec{B}}{\partial t} = \nabla \times (\vec{u} \times \vec{B}) + \eta \, \nabla^2 \vec{B} \qquad \text{Induction equation} \tag{2.7}$$

By manipulating (2.7) and (2.4) we can express the Lorentz forces (per unit volume) acting on the fluid as:

$$\vec{F} = \frac{1}{\mu}\Big(- \nabla\Big(\frac{B^2}{2}\Big) + (\vec{B} \cdot \nabla)\vec{B}\Big) \tag{2.8}$$

This is the additional sink term to be added the standard Navier Stokes equation.

The complete MHD system of equation is:

$$\nabla \cdot \vec{u} = 0 \qquad \text{Mass conservation} \tag{2.9}$$

eq. 2.2

$$\frac{D\vec{u}}{Dt} = -\nabla\frac{p}{\rho} + \nu\nabla^2\vec{u} + \frac{\Big(- \nabla\frac{B^2}{2}\Big) + (\vec{B} \cdot \nabla)\vec{B}}{\rho \, \mu} \qquad \text{Momentum conservation} \tag{2.10}$$

eq. 2.7

Which can be expressed in dimensionless form

$$\nabla \cdot \vec{u}^* = 0 \tag{2.11}$$

$$\nabla \cdot \vec{B}^* = 0 \tag{2.12}$$

$$\frac{\partial \vec{u}^*}{\partial t^*} + (\vec{u}^* \cdot \nabla)\vec{u}^* = -N\nabla p^* + \frac{1}{Re}\nu\nabla^2\vec{u}^* + \frac{N}{R_m}\Big(- \nabla\frac{B^2}{2}\Big) + (\vec{B}^* \cdot \nabla)\vec{B}^* \tag{2.13}$$

$$\frac{\partial \vec{B}^*}{\partial t} = \nabla \times (\vec{u}^* \times \vec{B}^*) + \frac{1}{R_m} \, \nabla^2\vec{B}^* \tag{2.14}$$

Here we can identify three dimensionless groups that physically describe the MHD flow behavior:

- Hydrodynamic Reynolds number $Re = \frac{v_0 \, \mathcal{L}}{\nu} = \frac{inertial \; forces}{viscous \; forces}$
- Interaction parameter $N = \frac{\sigma \, B_0^2 \, \mathcal{L}}{\rho v_0} = \frac{magnetic \; forces}{inertial \; forces}$
- Magnetic Reynolds Number $R_m = \frac{v_0 \, \mathcal{L}}{\eta} = v_0 \, \sigma \, \mu \, \mathcal{L} = \frac{magnetic \; advection}{magnetic \; diffusion}$

Where, v_0, $\mathcal{L}$, ρ stand for mean velocity and characteristic length scale of the flow, and density respectively.

The hydrodynamic Reynolds number gives an estimation on the how strong the inertial forces are with respect to viscous forces, and indicates if there is turbulence.
The Interaction parameter is relevant when $\vec{j}$ is primarily driven by $\vec{u} \times \vec{B}$ in Ohm's law (2.5), In that case we can approximate $|\vec{j}| \tilde{=} \sigma \, u \, B$,and consider the magnetic forces constituted only by Lorentz forces, $N = \frac{Lorentz \; forces}{inertial \; forces}$.
Another important dimensionless group comes from the combination of Re and N

- Hartmann number $Ha = (N \, Re)^{0.5} = \Big(\frac{Lorentz \; Forces}{viscous \; forces}\Big)^{0.5} = B \, \mathcal{L}\Big(\frac{\sigma}{\rho \, \nu}\Big)^{0.5}$

2.2 Induction-less approximation (low $\mathbf{Re_m}$)

When $\mathrm{Re_m}$«1, which is the condition encountered dialing whit fusion blanket MHD flows, the magnetic field can be considered as purely diffusive: any perturbation due to the fluid motion is smoothed out. Therefore the induced magnetic field $\vec{b}$ can be neglected, $\vec{B} = \vec{B_0}$ and, since the fluid motion no longer influences the magnetic field, equation (2.7) can be simplified

$$\frac{\partial \vec{B}}{\partial t} = \eta \, \nabla^2 \vec{B} \qquad \text{Induction-less equation} \tag{2.15}$$

We can also introduce the electric potential Φ field and rewrite equation 2.5 as follow

$$\vec{j} = \sigma \, (-\nabla\Phi + \vec{u} \times \vec{B}) \tag{2.16}$$

By applying divergence in both sides and considering the conservation of charge (2.1), we end up to the Poisson equation for the potential. Furthermore, we can introduce the electric potential Φ and rewrite equation 2.5

$$\nabla^2\Phi = \nabla \cdot (\vec{u} \times \vec{B}) \qquad \text{Poisson equation} \tag{2.17}$$

We will see that this formulation will result in a reduction of complexity and in a reduction of computing time for the numerical evaluation. This is mainly due to the different nature of the problem: solving (2.17) instead of (2.7) essentially means running a solver for a scalar instead a vector field. The dissertation will return on this topic in the next chapter regarding the implementation algorithms.
The next section is devoted to the description of the fundamental analytic results, that can be found in literature to which numerical codes will be compared.

2.3 Boundary conditions

Before describing the boundary condition for the electric potential, it is appropriate to introduce the wall conductance ratio which is defined as:

$$c = \frac{\sigma_w \, t_w}{\sigma \, \mathcal{L}} \tag{2.18}$$

where t_w is the wall thickness and σ_w, σ stands for the electrical conductivity for the membrane and the fluid, respectively. From that value we can identify the particular class of boundaries: perfectly conducting walls, characterized by c=∞, and electrically insulating walls (c=0). Beside the no slip condition for the velocity profile, one can define the boundary condition for the induced magnetic field as follows:

$$c \, \frac{\partial \, \vec{b}}{\partial \, \vec{n}} + \vec{b} = 0 \tag{2.19}$$

where n is the direction normal the wall surface.
Applying the induction-less approximation the boundary conditions are given for the electric potential ϕ. Considering the thin wall approximation ($\mathrm{t_w} << \mathcal{L}$) we can make a current balance at the wall as it is sketched in fig. 2.1 Finally, we end up to the following expression:

$$\vec{j} \cdot \vec{n} = \sigma \Big(\frac{\partial \phi}{\partial n} \Big) = \nabla_t \cdot (t_w \, \sigma_w \, \nabla_t \, \phi_w) \tag{2.20}$$

where ∇_t is the gradient orthogonal to the normal surface facing the fluid, so the right hand side represent the current flux going trough it.

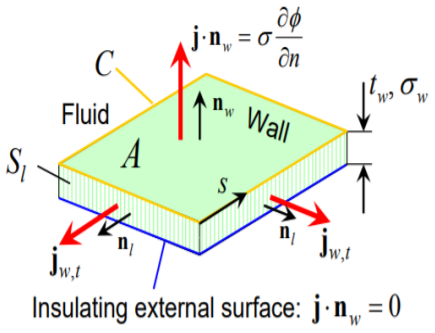

Figure 2.1: Current flux balance on wall membrane [15]

2.3.1 MHD between parallel plates - Hartmann flow

Hartmann firstly investigated the problem in 1937. As is shown in fig. 2.2. The problem consists of an electrically conducting fluid flowing under the influence of a pressure gradient, in the x-direction, through a rectangular cross section duct made by electrically insulated infinitely long in the z-direction, subjected to imposed magnetic field on (y) direction. The characteristic length scale $\mathcal{L}$ is represented by the half distance between the plates on the direction of the magnetic field. The analytic problem is 1D and the velocity profile develops in (y) direction. The literature always as Hartmann walls boundaries orthogonal to imposed magnetic filed in its honor.

https://www.overleaf.com/project/5c8f596416661e383a46e1

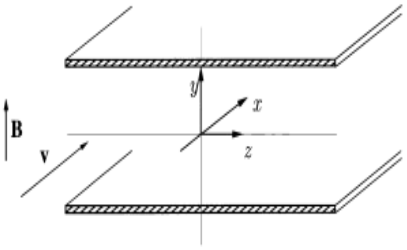

Figure 2.2: Hartmann flow [9]

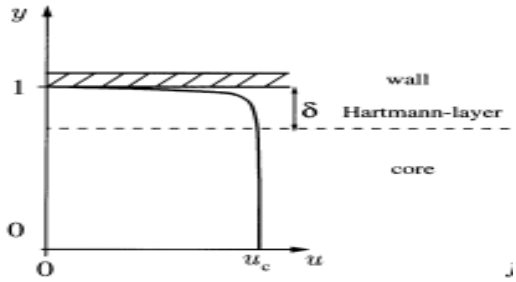

Figure 2.3: Hartmann boundary layer [9]

Fig. 2.3 shows the velocity(profile along (y) direction normalized to $\mathcal{L}$. The fluid velocity profile is almost flat, then suddenly fall to 0 in a thin boundary layer δ. Hartmann have found that:

$$\delta_h = \frac{\mathcal{L}}{Ha} = O\left(Ha^{-1}\right) \tag{2.21}$$

2.3.2 MHD in an electrically insulated duct - Shercliff case

Due to Shercliff (1952) [10], considers a square duct made by insulating walls. Hence side walls are now also considered. The problem is characterized by:

$$c_{Ha} = \frac{\sigma_{Ha}\, t_w}{\sigma\, \mathcal{L}} \to 0 \qquad \text{and} \qquad c_s = \frac{\sigma_s\, t_w}{\sigma\, \mathcal{L}} = 0 \tag{2.22}$$

The imposed magnetic field acts in the (y) direction, the problem is solved considering the velocity and inducted magnetic field on the axial direction x: $u = u_x(y,z); b = b_x(y,z)$. Equations 2.10 and 2.7 can be evaluated along the axial direction giving

$$\nabla^2 u_x(y,z) + \frac{1}{\mu\,(\sigma\,\eta)^{0.5}}\,\frac{Ha}{a}\,\frac{\partial\, b_x(y,z)}{\partial\, y} + \frac{\partial p}{\partial x} = 0 \tag{2.23}$$

$$\frac{1}{\mu\,(\sigma\,\eta)^{0.5}}\nabla^2 b_x(y,z) + \frac{Ha}{a}\,\frac{\partial\, u_x(y,z)}{\partial\, y} = 0 \tag{2.24}$$

For this class of problem, the solution is represented by series expansion of eigenfunctions. Fig. 2.4 (a) shows the electric current streamlines, that are generated by the interaction between the velocity and the imposed magnetic field. As a consequence, an induced magnetic field arise along the flow direction (current streamlines are $\vec{b}$ isolines), as well as an induced field electric acting on the side walls represented by symbols $\ominus$ and $\oplus$.

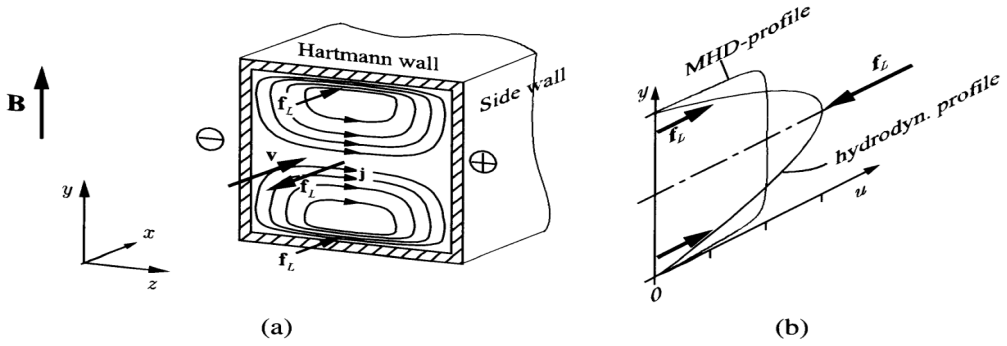

Figure 2.4: MHD flow for insulated square duct [9].

Consequently, a Lorentz force of the order of $\vec{j} \times \vec{B}$ is generated. Such force acts in opposite direction whit respect to the flow, and tends to damp it. This force decreases in magnitude closer to the insulating side wall, here the current streamlines deflects and tend to be parallel the imposed magnetic field $\vec{B}$, thus the product $\vec{j} \times \vec{B}$ tends to zero. Then the current lines curve again when meeting the insulating Hartmann wall, where the current lines flow in the opposite direction compared to the current line in the bulk of the flow. The Loretnz forces dominate the Hatmann layer resulting as a driving force for the fluid. (Figure 2.4 (b)).
Equation 2.21 is still valid for the evaluation of the Harmann side layer. As far as the side wall boundary layer δ_s is concerned, Shercliff found that:

$$\delta_s = \frac{\mathcal{L}}{Ha^{0.5}} = O\,(\,Ha^{-0.5}\,) \tag{2.25}$$

2.3.3 Hunt case

Hunt (1965) analyzed the case of rectangular ducts with insulated side walls and perfectly conducting Hartmann walls. The problem is characterized by:

$$c_{Ha} = \frac{\sigma_{Ha}\,t_w}{\sigma\,\mathcal{L}} \to \infty \qquad \text{and} \qquad c_s = \frac{\sigma_s\,t_w}{\sigma\,\mathcal{L}} = 0 \tag{2.26}$$

The same approach of Shercliff case is adopted for the treatment of momentum (2.10) and induction (2.7) equations. We end up to equations 2.23 and 2.24. The only difference is

given by the boundary condition for $\vec{b}$ at the different walls:

$$c\,\frac{\partial\,\vec{b}}{\partial\,n} + \vec{b} = 0 \tag{2.27}$$

Where n is the direction normal the wall surface. So the boundary conditions are:

$$\vec{b} = 0 \qquad \text{Insulated side walls} \tag{2.28}$$

$$\frac{\partial\,\vec{b}}{\partial\,n} = 0 \qquad \text{Perfectely conducing Hartmann walls} \tag{2.29}$$

2.4 Heat transfer

From the energy equation based on the frist law of thermodynamics, we can derive the equation considering all phenomena involved in MHD

$$\underbrace{\rho\, C_p \frac{D\,T}{D\,t}}_{\text{thermal gain}} - \underbrace{\beta\, T\, \frac{d\,p}{d\,t}}_{\text{expansions/expansions}} = \underbrace{\frac{\vec{j}^2}{\sigma}}_{\text{Ohmic heating}} + \underbrace{(\rho\, \nu\, \nabla \vec{v})}_{\text{Viscous dissipation}} + \underbrace{k\, \nabla^2\, T}_{\text{Heat fluxes}} + \underbrace{\rho\, S_{int}}_{\text{Volumetric generation}} \tag{2.30}$$

where C_p, T, β and k stands for heat capacity at constant pressure, temperature, thermal expansion coefficient and thermal conductivity, respectively.
In MHD flows for fusion blanket applications, we can easily neglect terms regarding thermal expansion/contraction, ohmic heating and viscous dissipation. Those terms are small enough compared to the others [12]. Hence equation 2.30 can be

$$\underbrace{\frac{\partial\, T}{\partial t}}_{\text{temperature transinet}} + \underbrace{\nabla \cdot (\vec{v}\, T)}_{\text{advective term}} = \underbrace{\alpha\, \nabla^2\, T}_{\text{Diffusive term}} + \underbrace{\frac{S_{int}}{C_p}}_{\text{Internal source}} \tag{2.31}$$

where $\alpha = \frac{k}{\rho\, C_p}$ represents the thermal diffusivity. The only sources considered are the heat fluxes applied to the walls and the internal heat generation due to neutron absorption and the exothermic reaction 1.8.

Chapter 3

Implementation in OpenFOAM and COMSOL

This chapter is devoted to the strategies adopted for MHD flow simulation. OpenFOAM and COMSOL have been used for this purpose. The first one is an open source, finite volumes software that is prone to field manipulation and operation: in fact, a string environment is available to the user who can directly implement his own code.
On the other hand, COMSOL Multiphysics is a commercial, finite elements code that allows to couple different physics modules within a GUI environment.
The aim of this chapter is to compare both the algorithms implemented in the two codes and the errors, as well.

3.1 OpenFOAM set-up - The PISO algorithm

The PISO (Pressure Implicit with Split Operation) presented by Issa (1985) [13]. The strategy is to solve the time dependent momentum equation by adopting the so called pressure-velocity coupling method. The time dependent transport equation, for one of the three component (i, j, k), for incompressible flow in absence of any momentum source except from the pressure gradient can be represented as:

$$\frac{\partial\, u_\mathrm{i}}{\partial\, t} = H(u_\mathrm{i}) - \nabla_\mathrm{i}\tilde{p} \tag{3.1}$$

where $\tilde{p}$ is the pressure divided by the density ρ, and the operator H contains the the advective and diffusive terms of the momentum equation. For a 2D (i, j) flow it yields:

$$H(u_\mathrm{i}) = \underbrace{-\frac{\partial\, u_\mathrm{i}\, u_\mathrm{i}}{\partial\, x_\mathrm{i}} - \frac{\partial\, u_\mathrm{j}\, u_\mathrm{i}}{\partial\, x_\mathrm{j}}}_{\text{advection}} + \underbrace{\nu\Big(\frac{\partial^2\, u_\mathrm{i}}{\partial\, {x_\mathrm{i}}^2} + \frac{\partial^2\, u_\mathrm{i}}{\partial\, {x_\mathrm{j}}^2}\Big)}_{\text{diffusion}} = [A(u)]\,\{u\} \tag{3.2}$$

The matrix [A(u)] contains the coefficients for the finite-difference representation of the spatial convective and diffusive fluxes and on brackets is highlighted its dependence on the velocity field, hence the non linear nature of the problem.
Since we are dealing with an implicit method, at each time step n, the partial time derivative of 3.1 is approximated as:

$$\frac{{u_\mathrm{i}}^{\mathrm{n}+1} - {u_\mathrm{i}}^{\mathrm{n}}}{\Delta t} = H({u_\mathrm{i}}^{\mathrm{n}+1}) - \nabla_\mathrm{i}\tilde{p}^{\mathrm{n}+1} \tag{3.3}$$

In order to achieve ${u_i}^{n+1}$ and $\tilde{p}^{n+1}$ an algorithm is performed which basically consist in a velocity predictor and, at least two pressure corrector. It can can be be summed up as follows:

1. Momentum predictor step

$$\frac{{u_i}^* - {u_i}^n}{\Delta t} = H({u_i}^*) - \nabla_i \tilde{p}^n \tag{3.4}$$

   Equation 3.4 is solved treating the pressure explicitly, ${u_i}^*$ is the predicted velocity field which does not satisfy the divergence free condition given by mass conservation 2.9.

2. First corrector step

$$\frac{{u_i}^{**} - {u_i}^n}{\Delta t} = H({u_i}^*) - \nabla_i \tilde{p}^* \tag{3.5}$$

$$\nabla {u_i}^{**} = 0 \tag{3.6}$$

   A new velocity field ${u_i}^{**}$, together with a new pressure $\tilde{p}^*$ are now evaluated in such a way to satisfy the continuity equation. It is important to notice that equation 3.5 is of explicit type of $H(u_i)$. By applying the divergence to it we end up to the pressure equation

$${\nabla_i}^2 \tilde{p}^* = \nabla H({u_i}^*) + \frac{\nabla {u_i}^n}{\Delta t} \tag{3.7}$$

   As $\tilde{p}$ is calculated, ${u_i}^{(**)}$ is computed

3. Second corrector step
   A new velocity field ${u_i}^{***}$, together with a new pressure $\tilde{p}^{**}$ are now evaluated by

$${\nabla_i}^2 \tilde{p}^{**} = \nabla H({u_i}^{**}) + \frac{\nabla {u_i}^n}{\Delta t} \tag{3.8}$$

The choice of corrector stages depends of the accuracy we want to achieve. From accuracy study it comes out that at least two corrector stages must be implemented in order to get accurate pressures. Hence, considering $k = 2$ as the number of corrector steps, ${u_i}^{***}$ approximates ${u_i}^{n+1}$ with approximation error that is of the order of Δt^4 and $\tilde{p}^{**}$ approximates $\tilde{p}^{n+1}$ with approximation error that is $O(\Delta t^3)$ [13].
Moreover, stability considerations needs to be taken since equation 3.5 is of explicit type. This will get the solution unstable for large time steps. To avoid instabilities without losing accuracy the strategy is to separate the operator H by its diagonal A_0 and off diagonal $H^{'}$ components $H(u_i) = H^{'}(u_i) + A_0 u_i$, and to treat the diagonal component implicit. The equation 3.5 can be rewritten as

$$\Big(\frac{1}{\Delta t} - A_0\Big){u_i}^{**} - \frac{{u_i}^n}{\Delta t} = H^{'}({u_i}^*) - \nabla_i \tilde{p}^* \tag{3.9}$$

3.1.1 Φ-PISO algorithm

This algorithm applies the induction-less approximation and implements equations 2.16 and 2.17 for the current and the electric potential, respectively.

If the pressure-velocity coupling method is an advantage from the point of view of the computational time used to solve the full set of MHD equations according to the induction-less approximation, some drawbacks have to be remarked. In particular, problems come when a collocated mesh with variables stored in the cell centroid is used. In such situation, especially at high Hartmann numbers, it can happen that the conservation of charge (2.16) is not respected. Conservative and consistent numerical schemes was developed by Ni e al. in 2007 [14].

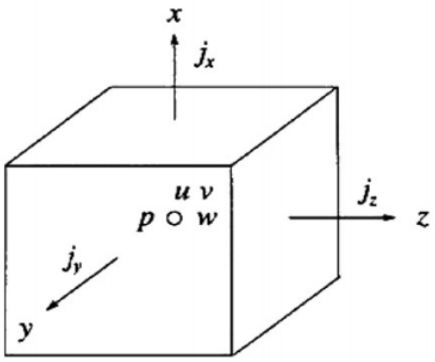

Figure 3.1: collocated grid system [14].

In Fig. 3.1 the collocated grid system is shown. All variables are stored at the cell center but the current density is evaluated at the cell face in such a way to satisfy

$$\int_{\Omega} \nabla \cdot \vec{j}\, d\Omega = \oint_{S} \vec{j} \cdot \vec{n}\, dS = \sum_{nf=1}^{nf} (\vec{j} \cdot \vec{n})_f\, S_f \tag{3.10}$$

where the subscripts Ω and S represents the cell control volume and the face surface and nf=6 represent the faces of the cubic cell.

The Algorithm can be summed up as follow

1. Creation of $\vec{u}$ field, pressure $\tilde{p}$, and velocity flux $\Phi_u = \int_S \vec{v} \cdot \vec{n}\, dS$. Initialization or the current density field $\vec{j}$ and Lorentz force per unit volume $\vec{L} = \vec{j} \times \vec{B_0}$. All those variables (except for the velocity flux) are stored at the cell centroid as we are dealing with collocated mesh.

2. Discretization of the momentum equation

$$\frac{\partial \vec{u}}{\partial t} + \nabla \cdot (\phi_u, \vec{u}) - \nabla^2(\nu, \vec{u}) - \frac{\vec{L}}{\rho} = -\nabla(\tilde{p}) \tag{3.11}$$

   In openFoam environment the user chooses the discretization scheme for the advective and diffusive term (i.e. Upwind, Central difference) and the time scheme for the transient (i.e. implicit/explicit Euler, Crank Nicholson etc.). The accuracy and the stability of the the solution are strictly affected by this choice. The important thing to note from eq. 3.11 is that the term containing the Lorentz forces depend on $\vec{j}$

hence on the velocity field by the Ohm's law. The Lorentz force term is considered as a source term of the momentum equation in a explicit way. Therefore, stability considerations must be taken into account even tough we choose time scheme apparently unconditionally stable.

3. Solve momentum equation (predictor step)

4. Entering the PISO loop with a fixed number of iteration and correct for pressure and velocity when is done.

5. Correct velocity field and update boundary conditions.

6. Evaluation the flux of $\vec{u} \times \vec{B}$ (second term RHS eq 2.16) at the cell faces for all mesh cells.
$$\psi_f = (\vec{u} \times \vec{B}) \cdot S_f \tag{3.12}$$

7. Solve Poisson equation for electric potential
$$\nabla^2 \phi = \nabla \psi \tag{3.13}$$

8. Computation of current density at the cell faces by applying the normal gradient of the potential on cell faces and adding the magnetic flux
$$j_f = -\nabla_n \phi \cdot S_f + \psi \tag{3.14}$$

9. Calculation of the current at the cell centroid by a volume weighted interpolation between cell face and centroid
$$\vec{j_c} = \frac{1}{\Omega_{cell}} \sum_{nf=1}^{nf} j_f (\vec{r_f} - \vec{r_c}) \cdot S_f \tag{3.15}$$

10. Evaluate the Lorentz force
$$\vec{L} = \vec{j_c} \times \vec{B} \tag{3.16}$$

11. Determine new time step;

12. Return to step 2

3.1.2 Stability considerations

As introduced in previous section, the velocity of the Lorentz force is treated implicitly in the algorithm. Neglecting the pressure gradient, The linearized 1D momentum equation discretized with a implicit Euler scheme in time and uniform finite difference spatial discretization can be seen as

$$\frac{{u_i}^{n+1} - {u_i}^n}{\Delta t} + v\left(\frac{{u_{i+1}}^{n+1} - {u_{i\text{-}1}}^{n+1}}{2\Delta x}\right) = \nu\left(\frac{{u_{i+1}}^{n+1} - 2{u_i}^{n+1} + {u_{i\text{-}1}}^{n+1}}{\Delta x^2}\right)\frac{\sigma B_0^2}{\rho}{u_i}^n \tag{3.17}$$

From this expression we can now identify the following quantities

- $C = \frac{v\Delta t}{\Delta x}$
- $D = \frac{2\nu\Delta t}{\Delta x^2}$
- $L = NC = \frac{\sigma B_0^2 \Delta t}{\rho}$

where N is the interaction parameter introduced in 2, C is the Courant number. We can rewrite eq. 3.17 as follow

$${u_i}^{n+1} - {u_i}^n + \frac{C}{2}\left({u_{i+1}}^{n+1} - {u_{i\text{-}1}}^{n+1}\right) = \frac{D}{2}\left({u_{i+1}}^{n+1} - 2{u_i}^{n+1} + {u_{i\text{-}1}}^{n+1}\right) - L{u_i}^n \tag{3.18}$$

For pure hydrodynamic flows, has been found that D plays a role on accuracy, so is neglected in stability analysis. The Courant number instead is key for stability and it should be less than 1, 0.5, 0.2 for 1D, 2D, 3D flows, respectively. In MHD, a Von Neamann stability study can be applied on eq. (3.18). It consists in applying the Fourier transform it. The velocity field in no longer time dependent but a complex quantity. We end up to

$${u_i}^{n+1}(k) = A(k, \Delta t, \Delta x){u_i}^n(k) \tag{3.19}$$

where A is the amplification factor, the condition that guarantee stability is $(|A|) < 1$. Mas de les Valls [12] has performed the analysis and found that the solution of 1D problem is stable for L < 2 even though we have high values of C and D.

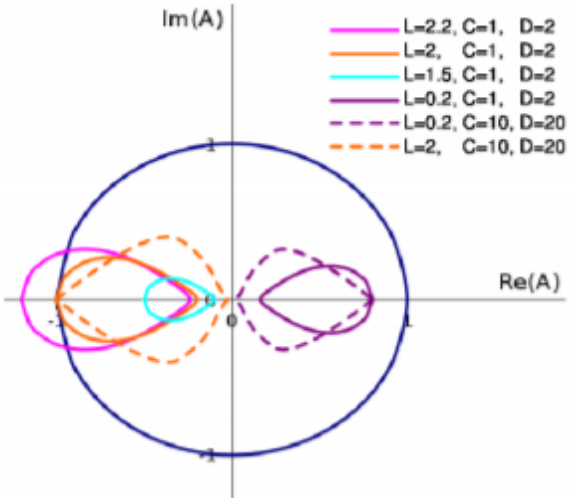

Figure 3.2: Locus of the amplification factor A [12]

3.2 COMSOL set-up an methodology

In COMSOL a steady state solver is implemented. The CFD module is modeled by setting a laminar and a electric current interface that by default contain conservation equations (i.e. eq. 2.1 and 2.9). The laminar interface is manipulated by adding the Lorentz force in the momentum equation as a source term. Similarly, a current density source is added in the second interface. The set of equation is now implemented and simulation can be run. The two interfaces are solved in a segregated way: giving in input the initialization values, Navier-Stokes equation is solved first and gives out the flow variables (i.e. velocity and pressure) that work as input for the electric potential equation. Solving the potential equation provides the Lorentz forces necessary for the next step Navier-Stokes equation, and so on. Iterations stop when computations converge to a set tolerance.

3.2.1 Coupling strategy

The momentum equation (2.10) and the Poisson equation for the electric potential (2.17) can be outlined as follows:

$$[H_1(\vec{u})]\,\{\vec{u}\} = [F_1(\vec{u})] \qquad \text{Laminar interface} \tag{3.20}$$

$$[H_2]\,\{\Phi\} = [F_2(\vec{u})] \qquad \text{Current interface} \tag{3.21}$$

$[\mathrm{H_1(U)}]$ and $[\mathrm{H_2}]$ are the global matrices, $\{\vec{u}\}$ and $\{\Phi\}$ are the global nodal variables. $[\mathrm{F_1(u)}]$ contains the pressure gradient and the Lorentz force while $[\mathrm{F_2(u)}]$ the product $\vec{u} \times \vec{B_0}$.
Once again, the two equation are solved sequentially through a segregated approach on Navier-Stokes and the electric potential equations. At the end of each iterative step for both the equations, the convergence criteria is checked and the above steps are repeated until the convergence criteria is achieved.

3.3 Geometry and mesh

A 10 cm (hydraulic diameter $d = 10$ cm) wide domain is modeled. It is half of the duct under study, taking advantage of the symmetry. The characteristic length of the problem is given by distance $a = 5cm$, which is the half length of the duct along the direction of the magnetic field (Fig. 3.3). Subsequently, a non-uniform collocated structured mesh as been generated. A key characteristic is the number of cells on each boundary layers: in this case, 26 cells cover each of the two side layers while there are 6 cells over the upper Hartmann layer. These numbers of cells for each boundary layer were taken from a grid convergence study conducted by Mistrangelo [19] in OpenFoam environment. For both the boundary layers the mesh is very fine at the wall and then gets progressively coarser, by a factor of 1.2 cell by cell, while getting away from the boundaries.

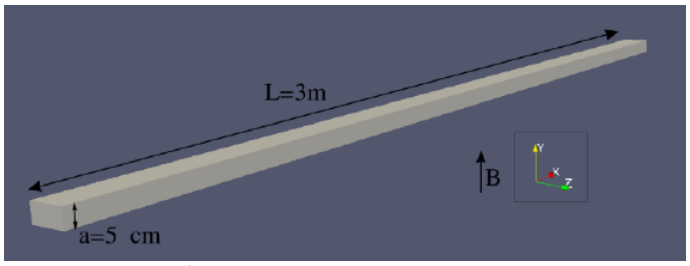

Figure 3.3: Pipe geometry.

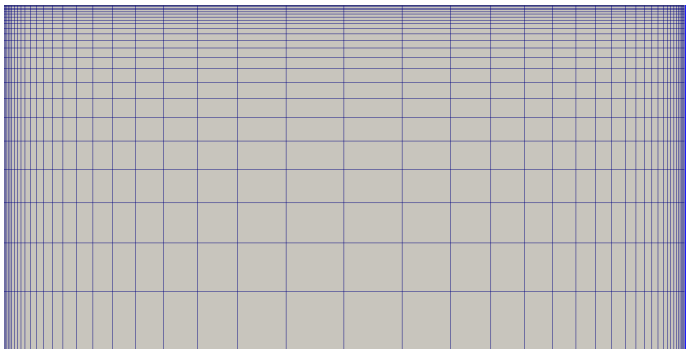

Figure 3.4: mesh OpenFOAM for Ha=10

Compared to OpenFOAM, COMSOL needs finer meshes in order to achieve the same tolerance value, especially at high Hartmann numbers. In this particular case, it has been found that at least 35 elements are needed at the side wall and 10 for the Hartmann one. In Fig.3.5 the mesh implemented for the 400 Ha case is shown.

3.3.1 Input Parameters

Laminar flow FLiBe has been modeled at constant temperature of 900 K at which it presents the properties listed in table 3.1.
The OpenFoam and COMSOL codes have been run for the Hunt problem (perfectly conducting Hartmann walls, electrically insulated side walls) with the analytical solution. Simulations are performed for four values of the Hartmann number (namely 10, 100, 400 and 1000) with related imposed magnetic fields (see table 3.2) acting on y direction, at an arbitrary pressure drop of 1 Pa/m acting on flow direction x, as a consequence the side wall direction is z. As ARC is still under design, this work is a preliminary study that sets up the basis for all the possible operation conditions of the tokamak, including the

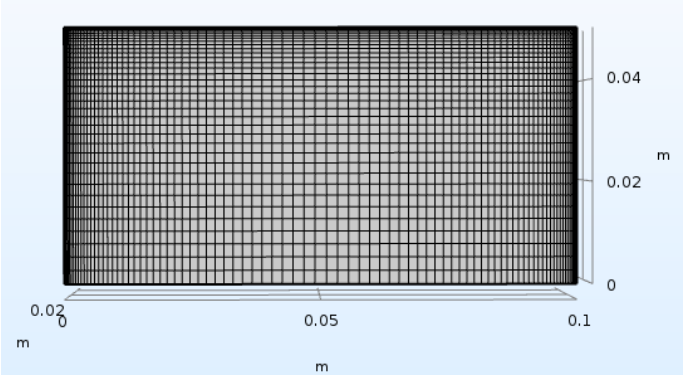

Figure 3.5: mesh OpenFOAM for Ha=400

Quantity	**Symbol**	**Value**	**Ref.**
density $[kg/m^3]$	ρ	2.15E+03	[17]
Viscosity [mPa s]	η	7.52	[17]
Electrical Conductivity [S/m]	σ	230	[18]
Specific heat [KJ/Kg/K]	c_p	2.38	[17]
Thermal conductivity [W/m/k]	k	1	[17]

Table 3.1: FLiBe's main thermo-physical properties

magnetic field, which is a key parameter for the Hartmann number. From these premises it has been chosen the wide range of the mentioned Ha number.
The characteristic parameters are grouped in table 3.2.

Case	**a**	**b**	**c**	**d**
Hartmann number	10	100	400	1000
Imposed magnetic field [T]	1.14	11.43	45.75	114.3
mesh elements OF [cells z,cells y]	[64,29]	[78,32]	[82,37]	[88,42]
mesh elements OF [cells z,cells y]	[78,35]	[86,38]	[98,45]	[110,59]
Pressure drop [Pa/m]	1	1	1	1
Mean velocity [m/s]	5.23E-3	1.30E-04	1.44E-05	3.46E-06

Table 3.2: Input data for the Hunt case for different Hartmann numbers.

In both simulation softwares periodic boundary conditions have been implemented. In OpenFoam the analytical mean velocity has been used as input parameter, hence the error is calculated on the computed pressure drop while in COMSOL the pressure drop is the input so the error is evaluated on computed mean velocity. Pressure and velocity field residuals tolerance has been set at 1e-4 in both the softwares.

3.4 Heat transfer

Once the code is validated, The heat transfer analysis has been conducted. In particular, has been considered condition the can be easily reproduced in practice:

- Square duct of 10 cm side and 3 m length.
- Laminar flow (Re=50), v_{mean}=0.1747 cm/s
- Imposed magnetic field of 3.46 T, corresponding to Ha=30
- Inlet temperature of 900 K and constant heat flux to the walls of 1000 W/m^2

Chapter 4

Results

In this chapter principal results are described. In particular the Hunt case has been developed according to the input data and the boundary conditions described in chapters 2 and 3.
First a benchmark among OpenFOAM, COMSOL and the analytical solution has been performed, for different Hartmann numbers (10, 100, 400, 1000). Then, a study case on the basis of ARC operational conditions (Ha=30) has been carried out.

4.1 Benchmark study

For each developed case, the following results are reported:
- the velocity 3-D configuration and isolines for the analytical solution computed using Matlab;
- the velocity field and the electric potential comparing numerical results obtained with OpenFOAM and COMSOL;
- the velocity profile at the side walls and Hartmann walls comparing the OpenFOAM, COMSOL and analytical solution results.
In addition, the comparison in terms of relative error between analytical and numerical solutions and computational time are reported to investigate and highlight the main advantages and drawbacks of the used software tools.

4.1.1 Hunt case with Ha=10

The first case presented is the one with the lowest Hartmann number taken into account, namely Ha=10. As mentioned, in Fig. 4.1 and 4.2 velocity results for the analytical solution are shown. More specifically they have been normalized to the channel's mean velocity. Even though Ha number is the lowest taken into account, it is possible to notice the typical M-shape velocity profile due to the Hunt's boundary conditions imposed (see paragraph 2.3.3). Figures 4.3 and 4.4 depict the velocity field obtained using OpenFOAM and COMSOL.
In figures 4.5 and 4.6 the electric potential is shown for both software tools. It highlights the charge concentration at the insulated walls.

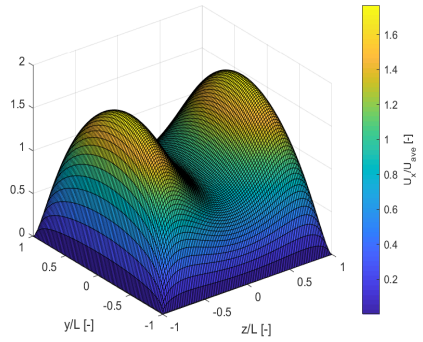

Figure 4.1: Analytical velocity, 3D isosurfaces output.

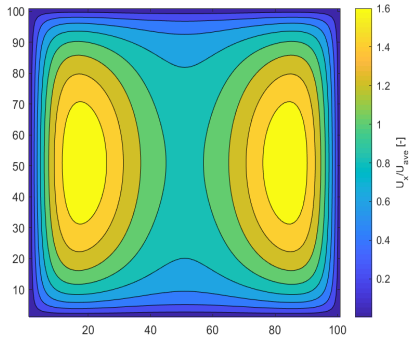

Figure 4.2: Analytical velocity, isolines output.

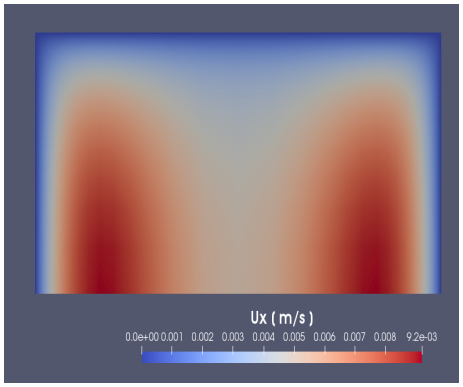

Figure 4.3: Velocity field OpenFoam.

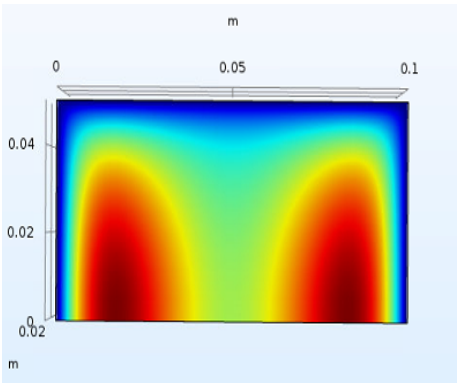

Figure 4.4: Velocity field COMSOL.

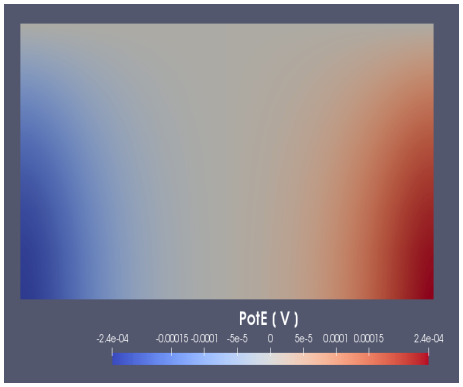

Figure 4.5: Electric potential, OpenFoam.

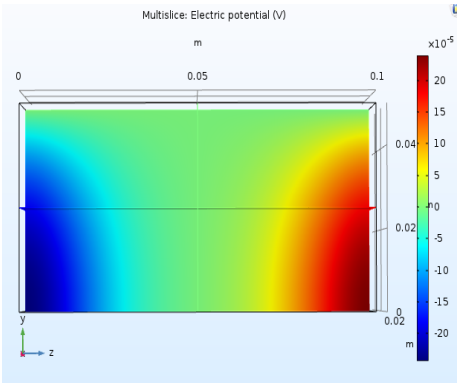

Figure 4.6: Electric potential, COMSOL.

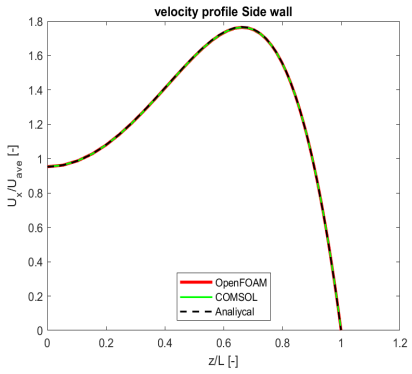

Figure 4.7: Velocity profile side walls.

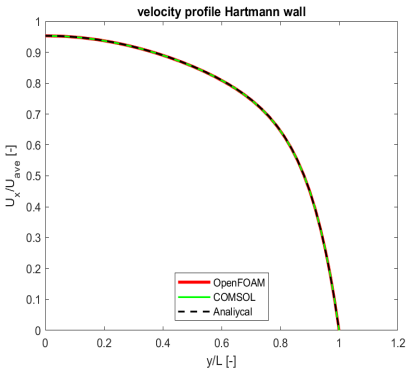

Figure 4.8: Velocity profile Hartman walls

In figures 4.7 and 4.8 the velocity profiles, normalized to the channel's mean velocity, at side walls and Hartmann walls relatively, are shown comparing OpenFOAM, COMSOL and the analytical solutions. In table 4.1 the relative error between the analytical and numerical solution for both codes are reported. It is possible to highlight that the error is fairly low. In addition, the computational time has been also indicated and it has been found to be over 4 times higher for COMSOL with respect to OpenFOAM.

software	**error [%]**	**elapsed time**
OF	0.0539	183.68 s
COMSOL	0.0737	758.4 s

Table 4.1: Relative error and computational time required for the two codes.

4.1.2 Hunt case with Ha=100

In this section the case with H=100 is reported. In Fig. 4.9 and 4.10 velocity results for the analytical solution are shown. More specifically they have been normalized to the channel's mean velocity. Here the M-shape velocity profile is more evident and the velocity peaks are closer and more concentrated on the side walls with respect to the previous case. Figures 4.11 and 4.12 depict the velocity field obtained using OpenFOAM and COMSOL. At Hartmann=100 the the fluid is subjected to higher Lorentz forces. As a consequence, the velocity peaks are stronger, roughly 6 times the mean velocity on the cross section of the duct. At the Hartmann walls the fluid is almost stagnant.
Figures 4.13 and 4.14 depict the electric potential obtained using OpenFOAM and COMSOL.

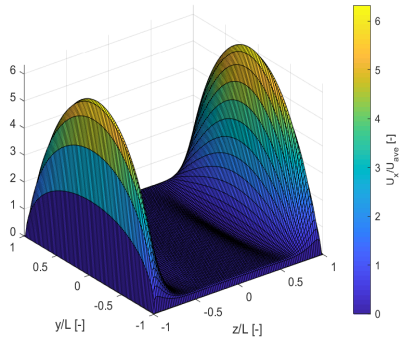

Figure 4.9: Analytical velocity, 3D isosurfaces output.

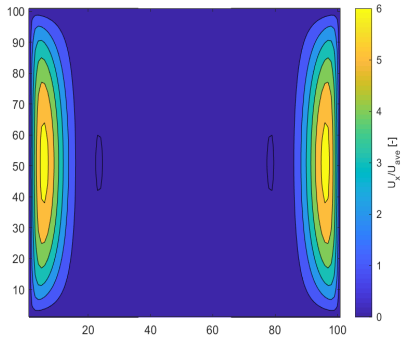

Figure 4.10: Analytical velocity, isolines output.

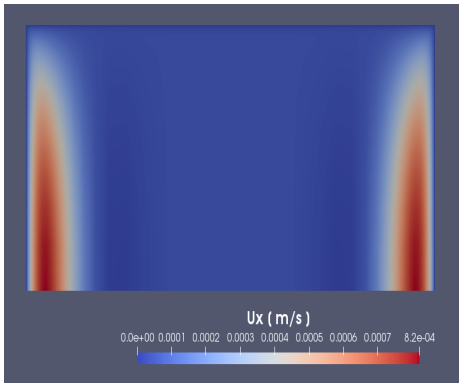

Figure 4.11: Velocity field OpenFoam.

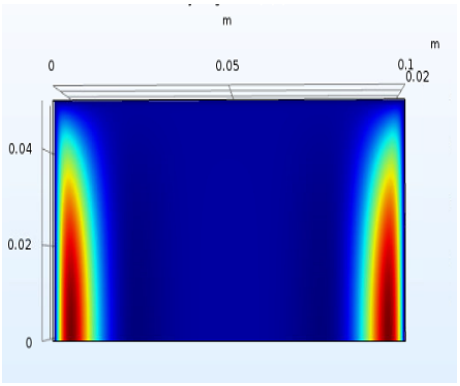

Figure 4.12: Velocity field COMSOL.

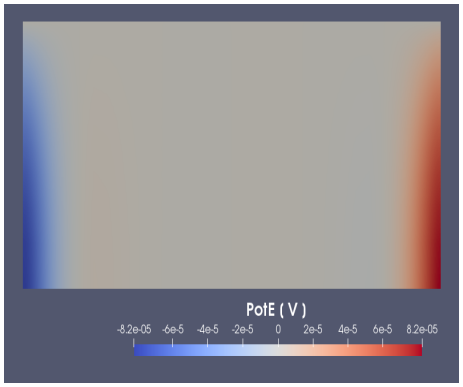

Figure 4.13: Electric potential, OpenFoam.

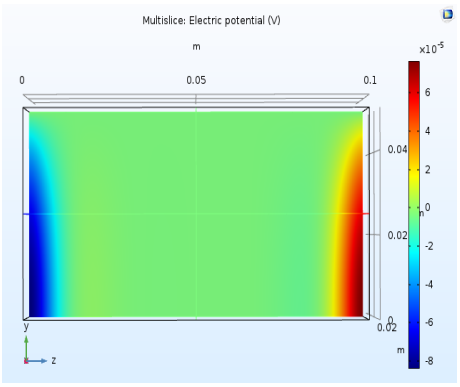

Figure 4.14: Electric potential, COMSOL.

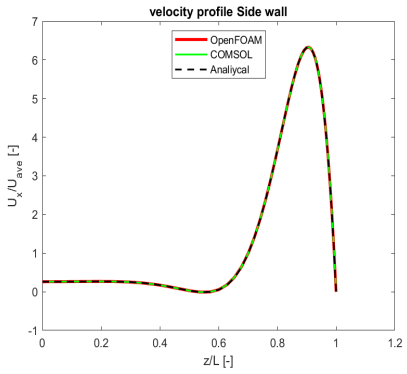

Figure 4.15: Velocity profile side walls.

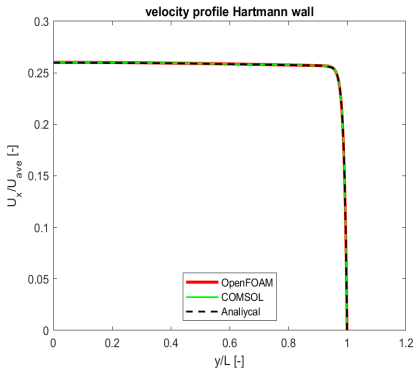

Figure 4.16: Velocity profile Hartman walls

In figures 4.15 and 4.16 the velocity profiles, normalized to the channel's mean velocity, at side walls and Hartmann walls relatively, are shown comparing OpenFOAM, COMSOL and the analytical solutions. In table 4.2 the relative error between the analytical and numerical solution and the computational time for both codes are reported. It is possible to highlight that the error is getting on the order of the unit of percentage. Concerning the computational time, COMSOL's one is, again, four times higher than OpenFOAM's.

software	**error [%]**	**elapsed time**
OF	0.8000	374.94 s
COMSOL	1.14	1527.6 s

Table 4.2: Relative error and computational time required for the two codes.

4.1.3 Hunt case with Ha=400

Here the solutions related to Hartmann number equal to 400 are presented. In Fig. 4.17 and 4.18 velocity results, normalized to the channel's mean velocity, for the analytical solution are shown. Figures 4.19 and 4.20 depict the velocity field obtained using OpenFOAM and COMSOL. Figures 4.21 and 4.22 display the electric potential obtained using OpenFOAM and COMSOL.

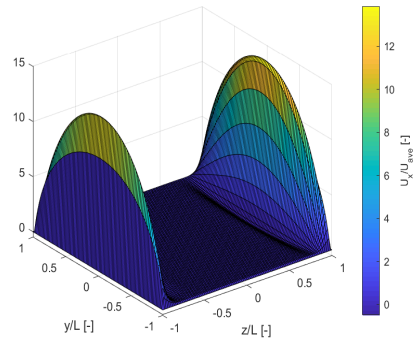

Figure 4.17: Analytical velocity, 3D isosurfaces output.

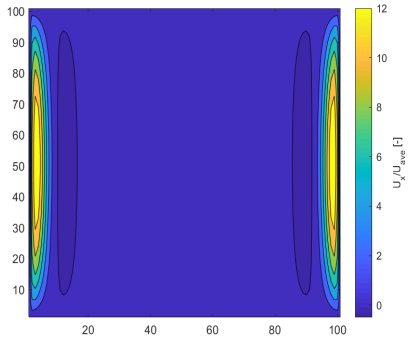

Figure 4.18: Analytical velocity, isolines output.

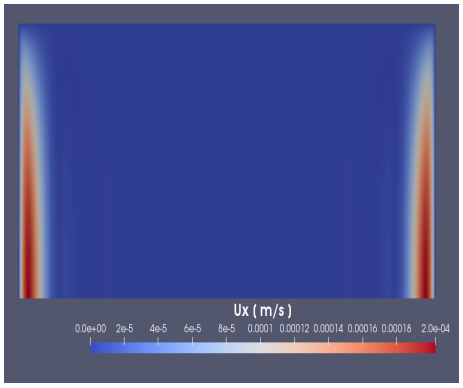

Figure 4.19: Velocity field OpenFoam.

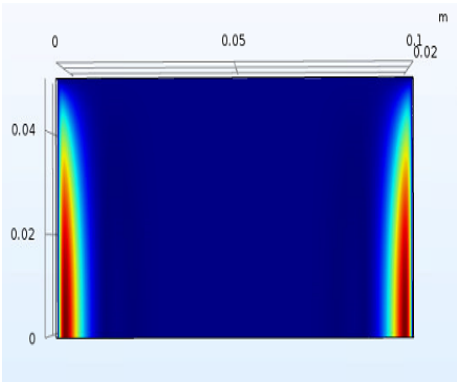

Figure 4.20: Velocity field COMSOL.

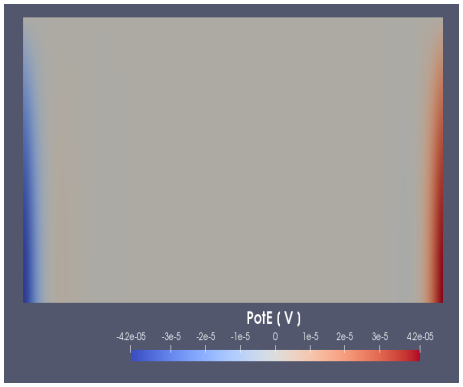

Figure 4.21: Electric potential, OpenFoam.

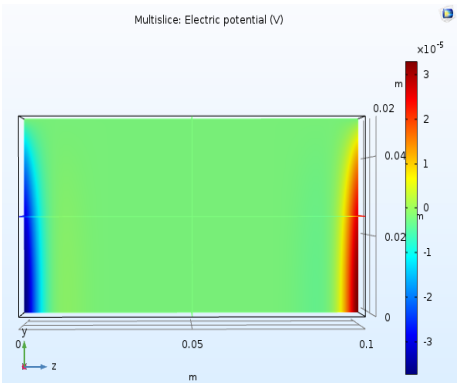

Figure 4.22: Electric potential, COMSOL.

In figures 4.23 and 4.24 the velocity profiles, normalized to the channel's mean velocity, at side walls and Hartmann walls relatively, are shown comparing OpenFOAM, COMSOL and the analytical solutions. In table 4.3 the relative error between the analytical and numerical solution and the computational time for both codes are reported. Errors are both on the order of the unit percentage, however COMSOL's one is relatively higher than OpenFOAMS, furthermore it requires a way longer computational time.

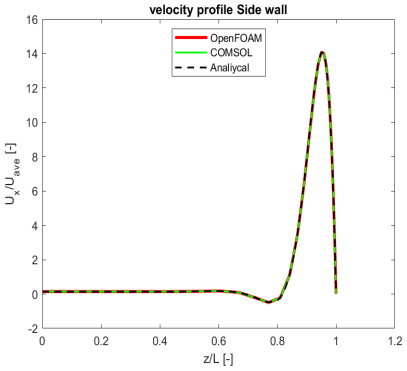

Figure 4.23: Velocity profile at the side walls.

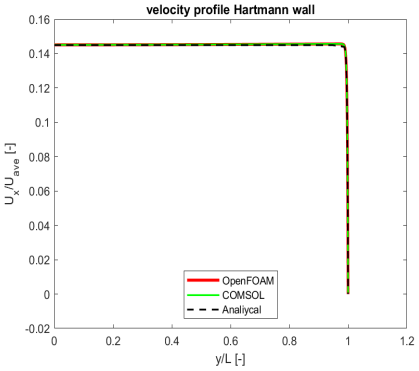

Figure 4.24: Velocity profile at the Hartman walls.

software	error [%]	elapsed time
OF	1.1097	811.34 s
COMSOL	1.784	2587.2 s

Table 4.3: Relative error and computational time required for the two codes.

4.1.4 Hunt case with Ha=1000

The last benchmark case shows simulation's outcomes related to Ha=1000. In Fig. 4.25 and 4.26 velocity field results for the analytical solution are shown. Once again, they have been normalized to the channel's mean velocity. Figures 4.27 and 4.28 depict the velocity field obtained using OpenFOAM and COMSOL. Finally, Figures 4.29 and 4.30 show the electric potential obtained using OpenFOAM and COMSOL.

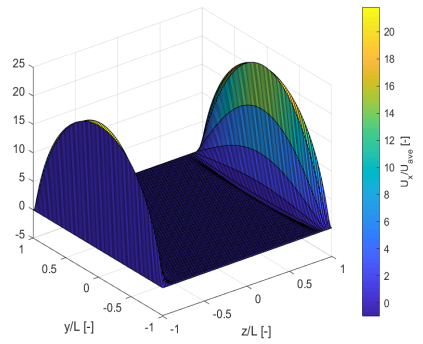

Figure 4.25: Analytical velocity, 3D isosurfaces output.

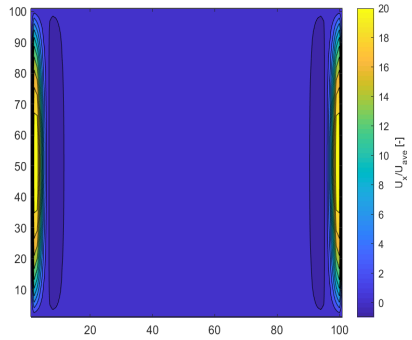

Figure 4.26: Analytical velocity, isolines output.

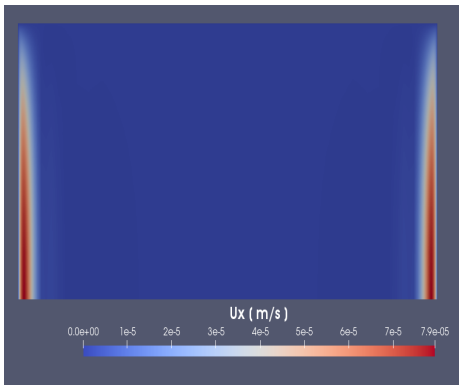

Figure 4.27: Velocity field, OpenFoam.

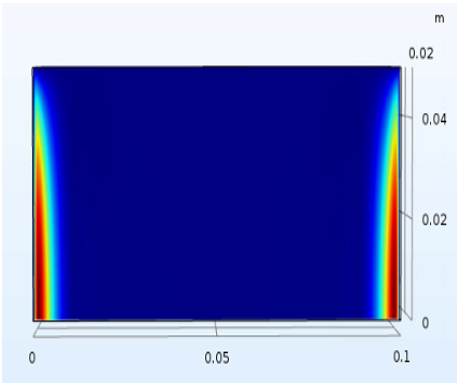

Figure 4.28: Velocity field, COMSOL.

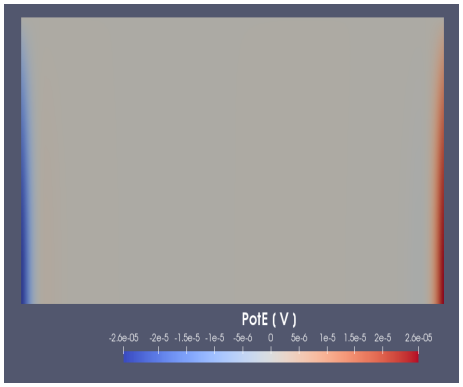

Figure 4.29: Electric potential, OpenFoam.

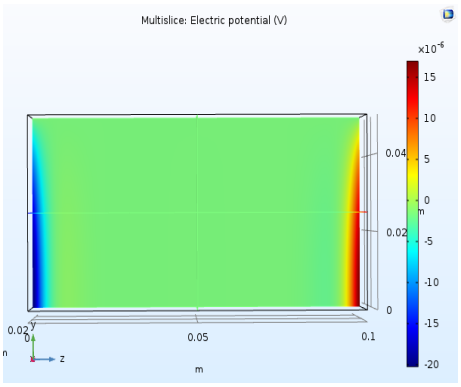

Figure 4.30: Electric potential, COMSOL.

In figures 4.31 and 4.34 the velocity profiles, normalized to the channel's mean velocity, at side walls and Hartmann walls relatively, are shown comparing OpenFOAM, COMSOL and the analytical solutions. In table 4.4 the relative error between the analytical and numerical solution and the computational time for both codes are reported. As the Ha gets higher, errors increase too. Of particular interest is the computational times over the Hartmann number increase: for OpenFOAM it remains roughly constant while for COMSOL it almost doubles with respect to the Ha=400 case scenario.

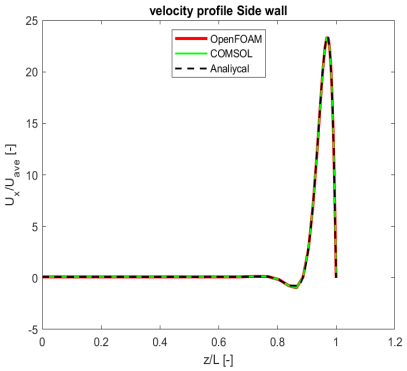

Figure 4.31: Velocity profile side walls.

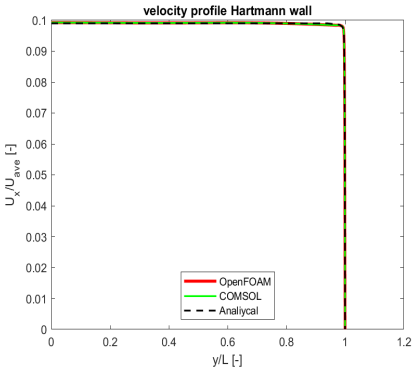

Figure 4.32: Velocity profile Hartman walls.

software	error [%]	elapsed time
OF	1.542	1165.3 s s
COMSOL	1.945	4550.4 s

Table 4.4: Relative error and computational time required for the two codes.

4.2 Heat transfer at Ha=30

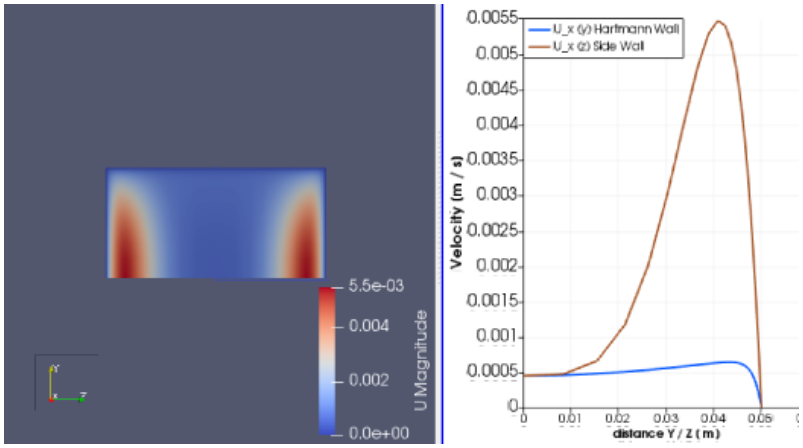

Figure 4.33: velocity profiles at outlet x= 3 m: Hartmann wall $U_x(y)$, Side wall $U_x(z)$.

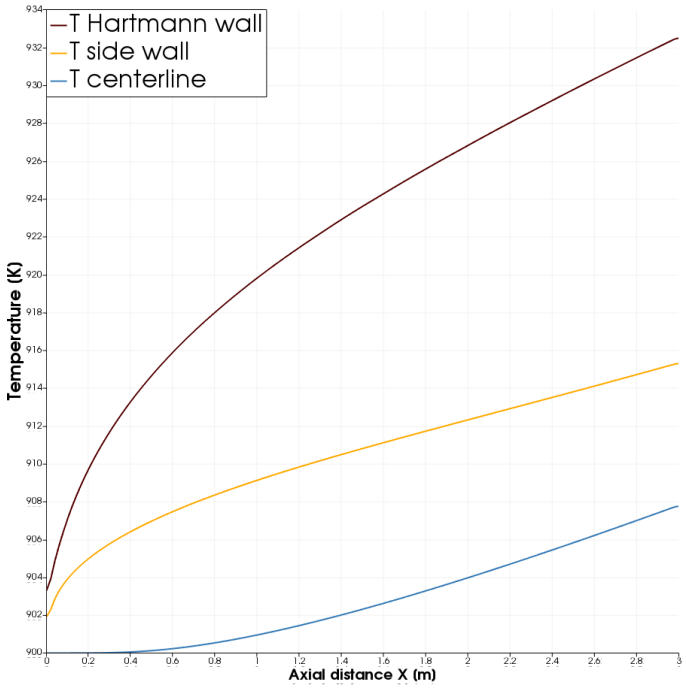

Figure 4.34: Temperature axial evolution

In figure 4.33 are shown the velocity profiles for each wall. Figure 3.34 depicts the temperature increase for the walls and the center line. It is shown that the jets near the side wall result on a better heat removal while the almost stagnant velocity at the Hartmann wall result on higher temperature.

Chapter 5

Conclusions

In order to simulate MHD flows for a molten salt blanket saving computational time several parameter must be taken into account.

The most important one is the magnetic Reynolds number. When this parameter is larger than 1 the induced magnetic field must be considered and the model must take into account all the parameters. Actually, fusion blankets are designed to operate at $R_{em} << 1$ and the induction-less approximation can be applied. It allows us to solve the Poisson equation for the scalar quantity "electric potential".

The second important parameter is represented by the Hartmann number, which is higher as the imposed magnetic field is increasing. This number gives an estimate of the boundary layer thickness and it is responsible for the high pressure drops.

In the ARC fusion reactor, although molten salts have relatively low values of the electrical conductivity, high values of Hartmann number can be reached due to the presence of strong toroidal magnetic field (up to 23 T in the inner board VV main chamber). Moreover, the geometry of the channel is supposed to have large dimensions, and this also implies high Hartmann numbers. Therefore, a reliable simulation code which foresees MHD flow with Hartmann numbers up to 2000 is essential in ARC's blanket design.

As Tungsten is the candidate material for the tank in which FliBe will flow, this work has been focused on electrically conducting ducts.

Two simulation tools have been considered in order to model this type of flow: OpenFoam and COMSOL.

The first one has been widely used for modeling liquid metal blankets with very good results. The OpenFOAM model is solving a transient for a pressure-based Navier-Stokes equation. In particular, a PISO-like algorithm has been utilized, since it is well known, from literature, as a robust and fast tool for getting accurate results. A drawback is represented by the restrictions on the time step which get higher as the Hartmann number increases. Other difficulties found using OpenFoam are represented by complex implementation of the equations to be solved, etc.

COMSOL, on the other side, is a user friendly tool thanks to the graphic user interface: the main differences between the two codes rely on the different way in solving the Navier-Stokes equations. In particular COMSOL relies on Finite Elements discretization while OpenFOAM takes advantage of the Finite Volumes method. They both can be used to study MHD problems under the simulated fusion raector regimes. Table 5.1 compares errors and elapsed time for each case. Two main results can be highlighted: firstly, to obtain roughly the same error, COMSOL needs quite higher computing times. Secondly, this phenomenon is becoming more relevant as the Hartmann number is increasing.

Ha	error OF [%]	Elapsed time OF	Error COMSOL[%]	elapsed time COMSOL
10	0.0539	183.68 s	0.0737	758.4 s
100	0.8000	374.94 s	1.14	1527.6 s
400	1.1097	811.34 s	1.784	2587.2 s
1000	1.542	1165.3 s	1.945	4550.4 s

Table 5.1: errors and elapsed time for each case.

A test case has been performed for Ha=30 in order to simulate with a coupled thermal-MHD model, an ARC relevant case. The model has shown the potential to obtain good results for an ARC relevant experiment, however further refinements of the OpenFOAM model and comparisons with a COMSOL model will have to be implemented in order to validate and improve the here presented results. In particular, future implementations could be devoted to study complex phenomena that occur during ARC operation including Q2D turbulence, internal heat generation ant tritium transport.

Bibliography

[1] Sorbom, B.N., Ball, J., Whyte, D.G. et al., *ARC: A compact, high-field, fusion nuclear science facility and demonstration power plant with demountable magnets* Fusion Eng.Des. 100 (2015)

[2] Kuang et al. *Conceptual design study for heat exhaust management in the ARC fusion pilot plant* 2018 Engineering and Design, vol. 100, pp. 378 405, nov 2015

[3] Freidberg, J., *Plasma Physics and Fusion Energy* Cambridge University Press, 2008.

[4] Theiler, Christian. (2011). *Basic Investigation of Turbulent Structures and Blobs of Relevance for Magnetic Fusion Plasmas.* 10.5075/epfl-thesis-5228.

[5] *https://en.wikipedia.org/wiki/Nuclearfusion*

[6] Friedman, I., *Deuterium content in natural waters and other substances* Institute for Nuclear Studies, University of Chicago (1953)

[7] Hartmann J. *Theory of the laminar flow of an electrically conductive liquid in a homogeneous magnetic field* Hg-Dynamics I. Levin & Munksgaard 1937

[8] P.A. Davidson. *An introduction to magnetohydrodynamics* Cambridge university press, 2001

[9] U. Müller and L. Bühler *Magnetofluiddynamics in channels and containers* Springer Science & Business Media, 2013.

[10] J.A. Shercliff. *Steady motion of conducting fluids in pipes under transverse magnetic fields* In Mathematical Proceedings of the Cambridge Philosophical Society, volume 49, pages 136–144. Cambridge University Press, 1953.

[11] J.C.R. Hunt. *Magnetohydrodynamic flow in rectangular ducts* Journal of Fluid Mechanics, 21(04):577–590, 1965.

[12] E.M. de les Valls. *Development of a simulation tool for MHD flows under nuclear fusion conditions.* PhD thesis, Dept. of Physics and Nuclear Engineering, Universitat Politecnica de Catalunya, 2011.

[13] R. Issa *Solution of the implicitly discretized fluid flow equations by operator-splitting* Journal of Computational Physics, 1965

[14] Ni M.J., Munipalli R., Huang P., Morley N. and Abdou M. *A current density conservative scheme for incompressible MHD flows at low magnetic Reynolds number Part I: On a rectangular collocated grid system* Journal of Computational Physics 227(1) 205–228, 2007.

[15] C. Mistrangelo. Simulation of magneto-hydrodynamic (MHD) flows in OpenFOAM. Presentation at NUMAP-FOAM Summer School University of Zagreb, http://powerlab.fsb.hr/ped/kturbo/OpenFOAM/SummerSchool2010/Chiara.pdf, 2010.

[16] Saad, Y. and Schultz M.H. *GMRES: a Generalized Minimal Residual Algorithm for Solving Non-Symmetric Linear Systems* SIAM J. Sci. Stat . Comput VOL. 7, pp. 856-869, (1986).

[17] D.-K. Sze, K. McCarthy, M. Sawan, M. Tillack, A. Ying, and S. Zinkle, Fusion Technology 39, 746 (2001).

[18] G. J. Janz, G. L. Gardner, U. Krebs, and R. P. T. Tomkins, Journal of Physical and Chemical Reference Data 3, 1 (1974).

[19] Chiara Mistrangelo. *Identification of requirements for accurate numerical MHD predictions and task work plan.* Final Report, EUROFUSION, 2014.

List of Figures

Appendix A

Analytic solution

A.0.1 Hartmann flow

$$V = v_0 \frac{cosh(Ha) - cosh(Hay/a}{cosh(Ha) - sinh(Ha)/Ha} \tag{A.1}$$

A.0.2 Shercliff and Hunt flow

$$V_z = \mu^{-1} V \Big(\frac{\partial p}{\partial z}\Big) a^2 \tag{A.2}$$

$$V = \sum_{k=0}^{\infty} \frac{2(-1)^k cos(\alpha_k \epsilon)}{l \alpha_k^3} (1 - V_2 - V_3) \tag{A.3}$$

$$V_2 = \frac{\Big(c_w r_{2k} + \frac{1-exp(-2r_{2k})}{1+exp(-2r_{2k})}\Big) \frac{exp(-r_{2k}(1-\eta)) + exp(-r_{2k}(1+\eta))}{2}}{2} \tag{A.4}$$

$$V_3 = \frac{\Big(c_w r_{1k} + \frac{1-exp(-2r_{1k})}{1+exp(-2r_{1k})}\Big) \frac{exp(-r_{1k}(1-\eta)) + exp(-r_{1k}(1+\eta))}{2}}{2} \tag{A.5}$$

$$N_k = (Ha^2 + 4\alpha_k^2)^{0.5} \tag{A.6}$$

$$r_{1k}, r_{2k} = 0.5(\mp HA + N)^{0.5} \tag{A.7}$$

$$\alpha_k = \Big(k + 0.5)\frac{\pi}{l} \tag{A.8}$$

where $\eta = x/a$, $\epsilon = y/a$, $C_w = \sigma_w$, $t_w/(\sigma a)$ $l = b/a$

Appendix B

Script for calculation of Hunt and Shercliff flows

```
clear all
close all
clc


Ni=100; % number of iteration for the asintotic solution
cw=10000; % conductance ratio of the hartman wall
%(cw=0 Sherckliff ; cw=inf Hunt cw=10 is sufficient)
%constants
mu_0=4*pi*1e-7; %[H/m] permeability vacuum
%thermophysical properties
T=900; %[k]
rho=2518-0.406*T; %[Kg/m3]
eta=1.16e-4*exp(3755/T); %[Pa*s]
nu=eta/rho;
sigma=(0.6*T-310); %[S/m]
%geometry
a=5e-2; %[m] half length along B
b=5e-2; %[m] half length orthogonal B
l=b/a; % aspect ratio
A=2*a*2*b; % Cross section [m2]
D_h=4*(2*a*2*b)/2/(2*a+2*b); %Hydraulic diameter [m]
%Laminar flow Re=100
% Re=100;
% vmean=Re*eta/rho/D_h; %[m/s]
Ha=1000; %Hartmann number
dpdx=-1; %pressure drop [Pa/m]
y=[-a:2*a/100:a]; % y direction discretized by 100 nodes
z=[-b:2*b/100:b]; % z direction discretized by 100 nodes
epsilon=z./a; % z vector normalized by a
csi=y./a; % y vector normalized by a

Vmean=0;
%evaluation of r1,r2,N,aplpha
```

```
for i=0:Ni
    alpha(i+1)=(i+0.5)*pi/l;
    N(i+1)=(Ha^2+4*alpha(i+1)^2)^0.5;
    r1(i+1)=0.5*(Ha+N(i+1));
    r2(i+1)=0.5*(-Ha+N(i+1));
    NV2(i+1)=cw*r2(i+1)+(1-exp(-2*r2(i+1)))/(1+exp(-2*r2(i+1)));
    NV3(i+1)=cw*r1(i+1)+(1-exp(-2*r1(i+1)))/(1+exp(-2*r1(i+1)));
    DV2(i+1)=0.5*cw*N(i+1)*(1+exp(-2*r1(i+1)))+...
        (1+exp(-2*(r1(i+1)+r2(i+1))))/(1+exp(-2*r2(i+1)));
    DV3(i+1)=0.5*cw*N(i+1)*(1+exp(-2*r2(i+1)))+...
        (1+exp(-2*(r1(i+1)+r2(i+1))))/(1+exp(-2*r1(i+1)));
    V2mean(i+1)=NV2(i+1)/DV2(i+1)*(1-exp(-2*r1(i+1)))/r1(i+1);
    V3mean(i+1)=NV3(i+1)/DV3(i+1)*(1-exp(-2*r2(i+1)))/r2(i+1);
    Vmean=Vmean+(2/l/alpha(i+1)^4)*((-1)^(i))*2*sin(alpha(i+1))*...
        (2-V2mean(i+1)-V3mean(i+1));
end
Vxmean=Vmean*(-dpdx/eta*a^2)/4; %mean velocity
Re=Vxmean/eta*rho*D_h; %reynolds number
V=zeros(length(csi),length(epsilon));
for k=1:length(csi)
    for j=1:length(epsilon)
        for i=0:Ni
            V2=NV2(i+1)/DV2(i+1)*0.5*(exp(-r1(i+1)*(1-csi(k)))+...
                exp(-r1(i+1)*(1+csi(k))));
            V3=NV3(i+1)/DV3(i+1)*0.5*(exp(-r2(i+1)*(1-csi(k)))+...
                exp(-r2(i+1)*(1+csi(k))));
            V(k,j)=V(k,j)+(1-V2-V3)*(2/l/alpha(i+1)^3)*((-1)^(i))...
                *cos(alpha(i+1)*epsilon(j));
        end
    end
end
Vx=-dpdx/eta*a^2.*V;%axial velocity
B=zeros(length(csi),length(epsilon));
for k=1:length(csi)
    for j=1:length(epsilon)
        for i=0:Ni
            B2=NV2(i+1)/DV2(i+1)*0.5*(exp(-r1(i+1)*(1-csi(k)))-...
                exp(-r1(i+1)*(1+csi(k))));
            B3=NV3(i+1)/DV3(i+1)*0.5*(exp(-r2(i+1)*(1-csi(k)))-...
                exp(-r2(i+1)*(1+csi(k))));
            B(k,j)=B(k,j)+(B2-B3)*(2/l/alpha(i+1)^3)*((-1)^(i))*...
                cos(alpha(i+1)*epsilon(j));
        end
    end
end
Bx=-dpdx*sqrt(sigma/mu_0)*a^2.*B; %induced magnetic field
```